Available online at www.sciencedirect.com
ScienceDirect
International Journal of Thermal Sciences 47 (2008) 52–67
International Journal of Thermal Sciences
www.elsevier.com/locate/ijts

Heat transfer in a reciprocating curved square duct fitted with longitudinal ribs

Shyy Woei Chang *, Che-Chih Lin, Jin-Shuen Liou

Thermal Fluids Laboratory, Department of Marine Engineering, National Kaohsiung Marine University, No. 142, Haijhuan Rd., Nanzih District, Kaohsiung, Taiwan, ROC

Received 14 July 2006; received in revised form 5 January 2007; accepted 5 January 2007

Available online 23 February 2007

Abstract

A set of experimental heat transfer data generated from a reciprocating square-sectioned curve duct fitted with longitudinal ribs along centerlines of duct walls is analyzed. Augmented Nusselt numbers in the static rib-roughened curve duct fall in the range of 1.2–1.45 times of smooth-walled curve-tube values as the longitudinal ribs trip the curvature induced vortices. Coupling effects of inertial, centrifugal and reciprocating forces in the rib-roughened reciprocating curved duct interact with buoyancy to exhibit synergistic influences on heat transfer. Local Nusselt numbers in the reciprocating test duct are in the range of 0.7–1.3 times of the non-reciprocation levels. Without buoyancy interaction, reciprocating Nusselt numbers decrease with the increase of the relative strength of reciprocating force within the present parametric conditions tested. Reciprocating buoyancy impacts enhance heat transfer and are inter-correlated with the pulsating force-effects. A set of empirical heat transfer correlation is derived to evaluate the individual and interactive effects of inertial, centrifugal and reciprocating forces, with and without buoyancy interaction, on overall heat transfer performance for piston cooling applications.
© 2007 Elsevier Masson SAS. All rights reserved.

Keywords: Reciprocating curved duct; Longitudinal rib; Piston cooling

1. Introduction

1.1. Industrial background

The power-to-weight ratio and thermal efficiency of a marine propulsive diesel engine are constantly increased by elevating the maximum cycle pressure and temperature. This thermodynamic incentive increases both mechanical and thermal loads acting on the hot components of engine. Internal cooling networks in a piston have become essential to maintain material temperatures at the sustainable levels and to facilitate effective lubrications. As coolant streams reciprocate with the piston, thermal fluid phenomena are modified from the static scenarios in the cooling network of a piston. Such reciprocation induced modifications vary with cooling configurations adopted. Currently available piston cooling configurations involve jet impingements [1], thermosyphons [2] and forced-convective channel flows [3]. Fig. 1 typifies the forced-convective piston cooling scheme for a marine propulsive diesel engine. As seen in Fig. 1, a pair of concentric passages in the piston rod channels the coolant stream into and out of the curved passages around the upper ring of piston crown. Centrifugal forces in these curved passages drive the cold coolant from the core region toward its outer edge. Dean-type vortices develop on the cross-sectional plan of each curved passage that generates peripheral heat transfer variations around the perimeter of each curved passage. As the reciprocation of piston is orthogonal to the flow direction in the curved passage, the reciprocating acceleration, which produces periodical body-forces acting on fluids, is established in the direction normal to the centrifugal force as indicated in Fig. 1. Structures of vortices and turbulences in these curved passages are affected by reciprocating forces in a cyclic manner. Flow and heat transfer physics in a reciprocating curved channel are the combined results of inertial, centrifugal and reciprocating force-effects along with buoyancy interactions.

* Corresponding author.
E-mail address: swchang@mail.nkmu.edu.tw (S.W. Chang).

1290-0729/$ – see front matter © 2007 Elsevier Masson SAS. All rights reserved.
doi:10.1016/j.ijthermalsci.2007.01.008

Nomenclature

A, B, a_s, b_s, f_a, f_b	constant coefficients	
a	amplitude of reciprocating motion	m
Cp_0	specific heat of coolant at flow entrance	$\mathrm{J\,kg^{-1}\,K^{-1}}$
D	diameter of curvature for curved duct	m
d	hydraulic diameter of test duct	m
Dn	Dean number $= Re\sqrt{d/D}$	
g	gravitational acceleration	$\mathrm{m\,s^{-2}}$
Gr	gravitational Grashof number $= g\beta_0\Delta T d^3/\upsilon_0^2$	
Gr_p	reciprocating Grashof number $= \omega^2 a\Delta T d^3/\upsilon_0^2$	
k_f	thermal conductivity of coolant at flow entrance	$\mathrm{W\,m^{-1}\,K^{-1}}$
Nu	reciprocating Nusselt number $= qd/(T_\mathrm{w} - T_\mathrm{f})k_\mathrm{f}$	
Nu_0	static Nusselt number	
Nu_∞	Dittus–Boelter Nusselt number	
Pr	Prandtl number of test coolant $= \mu Cp/k$	
Pu	pulsating number $= \omega d/W_\mathrm{m}$	
q	convective heat flux	$\mathrm{W\,m^{-2}}$
Re	Reynolds number $= \rho W_\mathrm{m} d/\mu_0$	
T_0	flow entry temperature	K
T_f	streamwise flow bulk temperature	K
T_w	wall temperature	K
ΔT	wall to fluid-bulk temperature difference	K
W_m	mean through flow velocity	$\mathrm{m\,s^{-1}}$
x	streamwise coordinate	m
z	coordinate in the direction of reciprocation	m
X, Z	dimensionless coordinates normalized by hydraulic diameter $(x/d, z/d)$	

Greek symbols

β	thermal expansion coefficient of coolant	$\mathrm{K^{-1}}$
ρ	coolant density	$\mathrm{kg\,m^{-3}}$
μ	dynamic viscosity of coolant	$\mathrm{kg\,s^{-1}\,m^{-1}}$
υ	kinematic viscosity of coolant	$\mathrm{m^2\,s^{-1}}$
θ	angular coordinate along the circumference of tube	degree
Φ	streamwise section along the curvature of test section	rad
ω	angular velocity of rotating disc creating reciprocating motion	$\mathrm{rad\,s^{-1}}$
Ψ, ξ, ζ	unknown functions	

Subscripts

0	flow entry condition
f	local fluids condition

Superscript

SW	smooth-walled channel

In our previous work [3], heat transfer characteristics in a reciprocating curved pipe with smooth wall were examined. Local Nusselt numbers in this reciprocating curved pipe were initially reduced from its static levels as reciprocating forces increased. This heat transfer reduction was followed by a subsequent recovery as the relative strength of reciprocating force further increased. Isolated buoyancy impacts in this reciprocating curved pipe improved heat transfers when the reciprocating force-effects remained as weak. Such an improving buoyancy effect on heat transfer was gradually weakened and turned into the impeding impact as the reciprocating force further increased. The combined inertial, centrifugal and reciprocating force-effects along with buoyancy interaction have caused the reciprocating-to-static Nusselt number ratios to fall in the range of 0.6–1.15. In the pursuit of heat transfer enhancements for piston cooling systems, several elements of surface roughness such as fins [4–7], twisted tape [8], ribs [9,10] and scales [11] are applicable for the forced-convective cooling configuration depicted in Fig. 1. Longitudinal fins in ducts with a variety of profiles such as rectangular, triangular, parabolic and undulated profiles are readily to fit in the curved piston cooling passage. Factors concerning the fin conductance, the extended heat transfer surface and the convective condition determined by fin profiles are inter-correlated to affect the heat transfer effectiveness of the longitudinal fin in a static duct [4–7]. Applying this heat transfer enhancing measure for piston cooling needs to consider the effects of reciprocation on thermal-fluid phenomena in the enhanced cooling passage and therefore on the problem of optimizing fin configurations. In this respect, our on-going research programs treat the square-sectioned longitudinal rib as the basic roughness element in a curved duct to augment the cooling effectiveness of piston. The present follow-up study focuses on the heat transfer augmentation provided by two pairs of square-sectioned longitudinal ribs with a rib-height to hydraulic-diameter ratio of 0.1 in a reciprocating curved square duct. Characteristics of forced heat convection in this enhanced reciprocating curved channel are examined through this experimental study.

Under the action of centrifugal force in a curved duct, the generation of cross-sectional secondary flows enhances the spatially averaged heat transfer with an amplified peripheral heat transfer variation [12]. Degrees of heat transfer augmentation along the outer edge of a curved tube are enhanced as Dean numbers increase; while the inner-edge heat transfer can be reduced from the straight tube level [13–16]. A numerical study of heat transfer in a curved duct with a longitudinal rib mounted on one wall demonstrates that the rib-induced heat transfer augmentation is attributed to the promotion of secondary vortex motion [10]. Enhancements of piston cooling performance using longitudinal ribs in curved channels require the consideration of reciprocating effects on heat transfer. There is no previous work looking into the synergistic effects of longitudinal ribs and reciprocation on heat transfer in a curved duct. Only a few of relevant studies examine the flow and heat transfer in static curved channels which are subject to externally imposed streamwise pulsating or oscillatory pres-

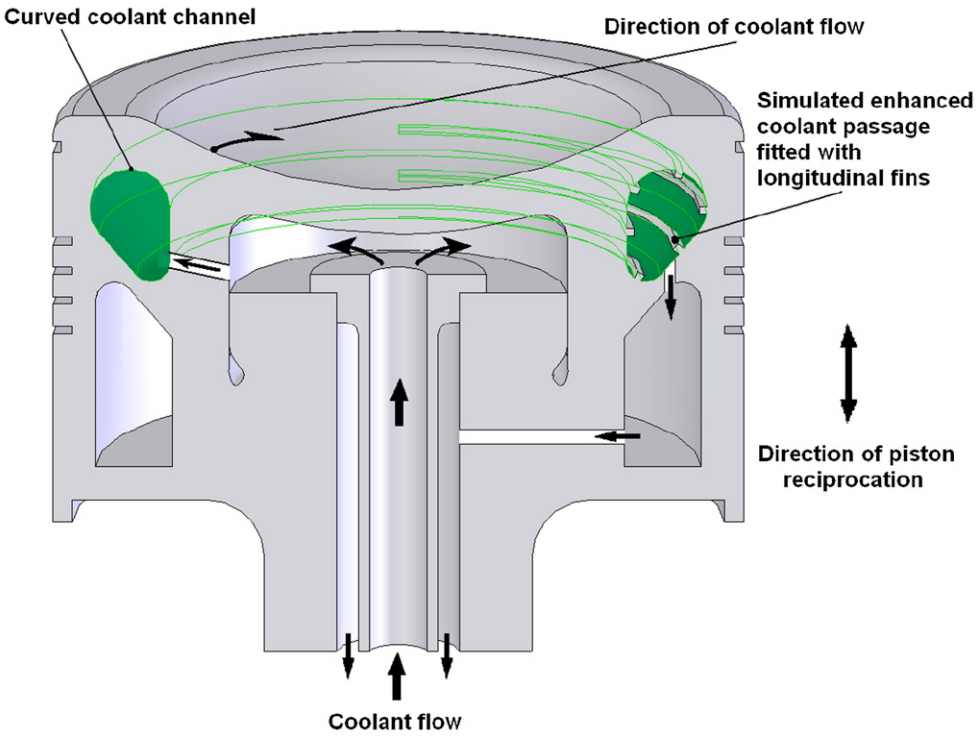

Fig. 1. Piston cooling networks of B&W L90MC diesel engine.

sure waves [17–20]. Studies of pulsating and oscillatory flows in a static curved channel offer the background knowledge for understanding the dynamic nature of secondary flows in a curved channel [17–20]. With through-flows subject to high frequency, time-sinusoidal pressure oscillations in a curved tube, a pair of secondary flow-cells in addition to Dean-vortices is developed in the in-viscid core [17]. With low-frequency oscillatory flows in a static curved pipe, the growth and decline of Dean-type vortices are accompanied with secondary flow-reversals during each pulsation cycle [18]. Oscillatory or pulsating forces in a static curved tube also modify the vortical flow structures form Dean-type secondary vortices to the time-dependent dynamic vortical flow structures. These time-varied cyclic secondary flows promote the transverse fluid mixing between the central and wall regions in a curved tube. Such a dynamic vortical mixing process due to flow pulsations in a curved tube has led to the Prandtl number (Pr) effect on heat transfer augmentations [18]. Dean numbers need to be considerably increased before the additional heat transportations attributed to the unsteady transverse mixing become dominant. Time-averaged Nusselt numbers in a static curved tube with oscillatory flows are considerably enhanced for the flow conditions with high Pr, high oscillating amplitudes and low oscillating frequencies [19,20].

Studies of turbulent flows over a spanwisely oscillating wall are also relevant to the orthogonal-mode reciprocating flow [21–24]. In a channel with one sidewall oscillating in the spanwise direction, the near-wall logarithmic velocity profiles are shifted upwards from the oscillating wall so that the viscous sublayers are thickened. In such a spanwisely oscillating channel, turbulence intensities across the boundary layer are reduced. These combined effects reduce the skin-friction drag of the turbulent boundary layer due to spanwise-wall oscillations [21–23]. Another investigation [24] focuses on the drag reduction in the channel with a spanwisely oscillating wall. These authors demonstrate that the spanwise vorticity is generated by the periodic Stokes layer developed over the oscillating wall [24]. The generation of such spanwise vorticity reduces mean velocity gradients across wall boundary-layers and hampers the longitudinal vortices in the viscous sublayer that are stretched in the streamwise direction [24]. As a result, the streamwise vorticity is reduced, which consequently weakens the near-wall bursting activity for turbulent channel flow. Above inter-correlated mechanisms induced by spanwise wall-oscillations [24] raise the possibility of heat transfer reduction in a curved tube that reciprocates orthogonally. Experimental evidences collected from our previous work [3] verify this hypothesis by demonstrating the heat transfer impediments from static references due to orthogonal mode reciprocations.

The present experimental study examines the variations of streamwise as well as peripheral Nu distributions in the static and reciprocating curved square duct fitted with a longitudinal rib along the centerline of each duct wall. The strategic aim is to unravel the characteristics of heat convection in this reciprocating rib-roughened curved duct via a parametric analysis based on the experimental data generated. The parametric analysis unravels the individual and interactive influences of centrifugal and reciprocating forces with and without buoyancy interaction on heat convection, which assists to derive heat transfer correlations for piston cooling applications.

2. Experiments

2.1. Governing dimensionless flow parameters

The parametric analysis of present problem requires the identification of controlling dimensionless flow parameters. This is achieved by analyzing the reciprocation induced complexities in the conservation type of flow equations. Modifications of heat transfers in a reciprocating duct from its static conditions are originated from the reciprocating acceleration of duct, which interacts with the density field of flow to create pulsating body forces and buoyancy interactions. Derivations of dimensionless momentum and energy equations expressed relative to a reciprocating reference frame identify these dimensionless groups that signify the heat transfer physics in a reciprocating channel. The functional relationship between local Nusselt number (Nu) and the controlling dimensionless groups for flows through a reciprocating curved duct is identified as Eq. (1) [2].

$$Nu(\theta, X) = \Psi\{Re, Dn, Pr, Pu, Gr, Gr_p, \text{ Boundary conditions}\} \quad (1)$$

All dimensionless groups in Eq. (1) and their constitutional structures are as defined in the nomenclature section. Coordinates θ and X are in the angular and streamwise directions of a curved duct respectively. Boundary conditions in Eq. (1) include the geometrical, heating and flow-entry conditions, which are specified by the configurations of heat transfer test module. Due to temperature variations of coolant as a result of heat transfer, local Pr values under present test conditions vary within a maximum range of $\pm 2.16\%$. Consequent Pr effects on heat transfer brought by this small Pr variation are negligible so that the present investigation excludes Pr from Eq. (1). Heat transfer impacts in association with each dimensionless group in Eq. (1) are examined by systematically varying the dimensionless flow parameter with the others in Eq. (1) remaining unchanged. Eq. (1) includes two reciprocation related flow parameters, namely the pulsating (Pu) and reciprocating Grashof (Gr_p) numbers that respectively quantify the ratio of reciprocating to inertial forces and the relative strength of reciprocating buoyancy [25]. It is worth noting that the buoyancy interaction in a reciprocating channel takes place in a virtually unsteady flow field. Reciprocating Grashof numbers (Gr_p) index a different mode of buoyancy interaction from those developed in steady flows with a sufficient time to generate the stable buoyancy force as well as the matured thermal boundary layers. A detailed description in this respect has been previously reported [2]. As the order of Gr/Re^2 for the present study is less than unity, the gravitational free-convection effects can be neglected. This will be re-confirmed by the zero-reciprocation results which show the indistinguishable Gr impacts on Nu_0 variations for the present data range. As a result, the impacts of free-convection within the tested ΔT range are not noticeable so that the flow parameter Gr is discarded from Eq. (1) for the present investigation.

As a result of buoyancy interaction, isolated Re (Dn) and Pu effects on heat transfer are not feasible to be unraveled using the direct Nu measurements. A finite wall-to-fluid temperature difference is needed to define the experimental Nu data. Such a wall-to-fluid temperature difference inevitably incurs the buoyancy impact on heat transfer that affects the measured Nu value. This formulates a practical difficulty as the Nu data with zero buoyancy level ($Gr_p = 0$, $Pu \neq 0$) is not feasible to be generated by heat transfer experiments due to the finite value of thermal expansion coefficient for a real fluid. In such a limiting case with a vanished wall-to-fluid temperature difference in a reciprocating duct, Ψ value in Eq. (1), expressed as the corresponding Nusselt number, reflects the combined Re (Dn) and Pu effects on heat transfer without any buoyancy interaction. This additional set of zero buoyancy heat transfer data is inferred by extrapolating a family of Nu measurements taken at a specific Re (Dn) or Pu but with different wall-to-fluid temperature differences into the zero buoyancy asymptotes. Subsequent analysis of isolated Re (Dn) or Pu impacts on reciprocating heat transfer without buoyancy interaction is performed using this set of zero buoyancy heat transfer data.

2.2. Apparatus

Mechanical details of the reciprocating rig, instrumentations for measurements of flow, heating-power and temperature along with methods of data acquisition and processing have been extensively described in previous papers [3,8,9]. In the interest of brevity, the reciprocating test rig is described briefly. This rig is configured to provide a test envelop that reciprocates at frequencies up to 2.5 Hz. Adjustable reciprocating motions are created by a crank-wheel mechanism. The translating velocity of reciprocating rig driven by the rigid crank-wheel mechanism is not a constant value but a skewed temporal sinusoidal function, which is attempted to simulate the dynamic motion of a real piston. The test coolant (air) for this study is pressurized by IWATA SC 175C screw-type compressor unit. Coolant flows are dehumidified and cooled to ambient temperatures that are channeled through a set of pressure regulator and filter, a pressure transducer, a Tokyo Kesio mass flow meter and a needle valve to measure and control the mass flow rates. Coolant's mass flow rate is frequently adjusted to compensate variations of coolant properties in order to maintain the deviations of Re and Pu from the targeting values within $\pm 1\%$ at the flow entrance of test section. This adjustment is achieved by feeding the relevant flow measurements into an on-line monitoring program that calculates Re and Pu at the flow entrance of test section. The metered airflow is then entered the straight section of calming duct with an equivalent length of 10 hydraulic diameters of test duct prior to entering the curved heat transfer test section.

The heat transfer test module is mounted on the reciprocating rig with the airflow direction in orthogonal to the reciprocating direction as seen in Fig. 2(a). Constructional details of heat transfer test module are depicted in Fig. 2(b). As illustrated in Fig. 2(b), the curved square test channel is constructed by assembling four 20 mm thick Teflon plates (1)–(4). Two curved Teflon plates (1)(2) are sandwiched between two 500×600 mm rectangular Teflon plates (3)(4) to form a 20×20 mm square-

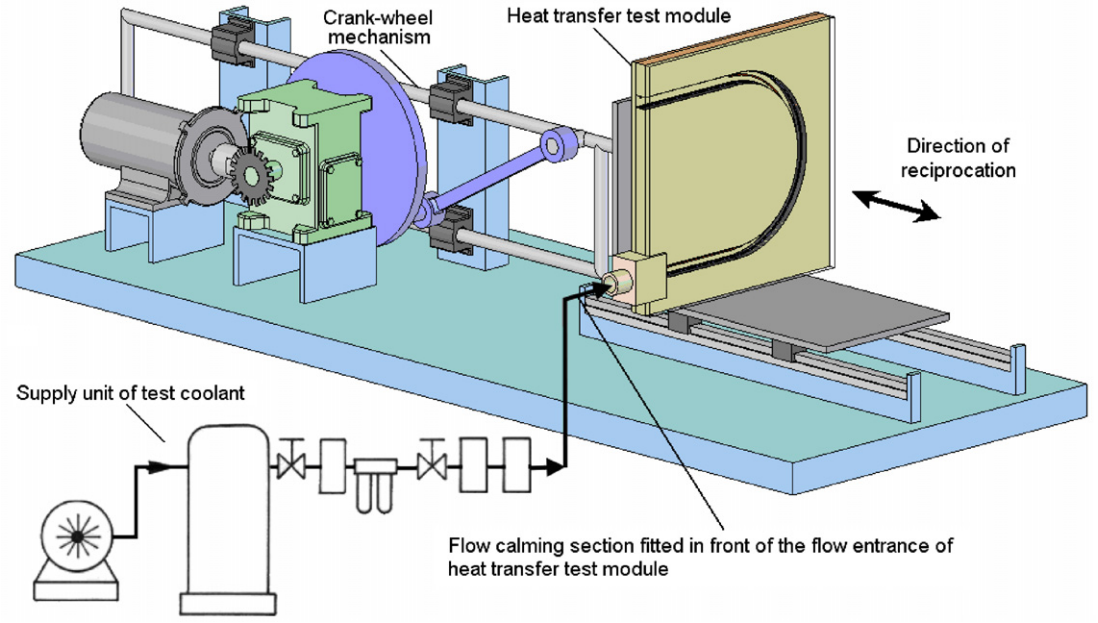

(a)

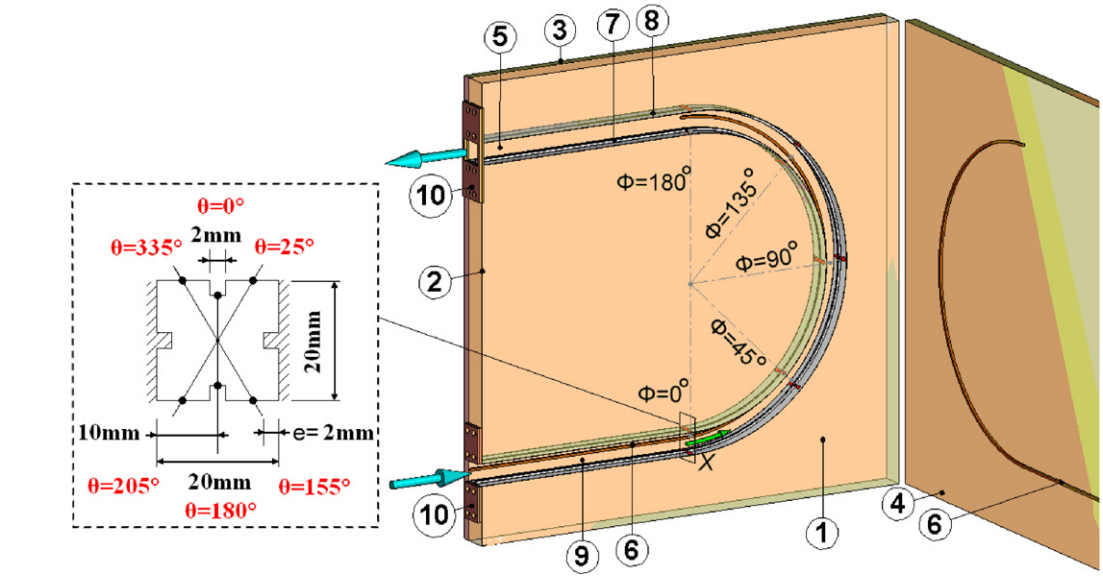

(1) Teflon plate with concave contour
(2) Teflon plate with convex contour
(3) (4) End Teflon plate
(5) Square sectional curved channel
(6) Square sectioned longitudinal rib on Teflon plate
(7) (8) Stainless steel heating foils
(9) Square sectioned longitudinal rib of heating foil
(10) End copper plate

(b)

Fig. 2. Experimental apparatus (a) reciprocating test rig (b) heat transfer test module.

sectioned curved channel (5). Along the centerline of the curved channel on the surfaces of Teflon plates (3)(4), a 2 × 2 mm square-sectioned longitudinal rib (6) is milled on the surface of each Teflon plates (3)(4). Each of two 20 mm wide, 0.1 mm thick stainless steel foils (7)(8) is forged with a 2 × 2 mm square-sectioned longitudinal rib (9) along its centerline to formulate the heated inner and outer walls of the test channel. The complete square-sectioned curve duct fitted with a longitudinal centerline rib on each of its constituent wall is obtained by assembling four Teflon plates (1)–(4) and two stainless steel heating foils (7)(8). Each inner and outer rib-roughened walls of the test channel (5) is heated with a basically uniform heat flux; while the rib-roughened upper and bottom sidewalls are thermally insulated. The hydraulic diameter of test channel (d) is defined as 20 mm. The diameter of curvature for the square-sectioned curved test channel (D) is 270 mm, which gives a di-

mensionless D/d ratio of 13.5. The rib-height (e) to hydraulic-diameter (d) ratio of each longitudinal rib is 0.1. The test fluid is channeled through a straight flow calming section of 200 mm (9) prior to entering the curved test section. Two pairs of straight centerline longitudinal ribs are also fitted in this flow calming section (9).

System reciprocations involve the reciprocations of curved test channel and the straight flow-calming section as seen in Fig. 2(a). Two end copper terminals (10) connect the stainless-steel heating foils on the entry and exit sections of the test channel (5) through which the adjustable high-current, low-voltage electrical power is supplied. Electrically heating fluxes are thus uniformly generated by stainless-steel foils to simulate basically uniform heat flux heating conditions on the inner and outer walls of test channel. External heat losses from the heating foils are minimized by the Teflon plates.

Thirty thermocouples measuring wall temperatures of test channel are spark-welded on the back surfaces of heating foils at locations specified in Fig. 2(b). Streamwise (X), angular (θ) and circumferential (Φ) coordinate systems are defined in Fig. 2(b). Origins of present coordinate systems with $X = 0$ and $\Phi = 0^\circ$ are positioned after the straight flow calming section. The positive angular (θ) direction is defined as the clockwise direction with $\theta = 180^\circ$ at the outer edge of test duct. Following this manner of coordinate definition, reciprocating forces are acting along the direction toward the spots of $\theta = 90^\circ$ and 270°. Angular wall-temperature profiles on five cross-sectioned planes of $\Phi = 0^\circ$, 45°, 90°, 135° and 180° of the curved test section are measured. At each measured circumferential section, six thermocouples are installed along the perimeter of heating foils at the angular locations of $\theta = 0^\circ$, 25°, 155°, 180°, 205°, and 335°. These angular locations precisely correspond to two rib-tops and four mid-rib locations as indicated in Fig. 2(b). Ceramic cements provide the essential adhesion to secure each thermocouple bead at the precise location. Streamwise as well as angular variations of wall temperatures due to combined effects of duct-curvature and orthogonal-mode reciprocation are recorded by these thermocouples. Two additional thermocouples penetrate into the core of the flow path to measure the bulk-flow entry and exit temperatures. All these temperature measurements are monitored and recorded by a PC via the Net-Daq Fluke Hydra 2640A data logger. Prior to heat transfer tests, all the thermocouples are calibrated in a constant temperature bath to ensure the measurement accuracy of ± 0.1 K. Local coolant properties such as β_0, Cp_0, k_0, and μ_0, which are used to evaluate the dimensionless parameters such as Gr_{p0}, Pu_0, Dn_0 and Re_0 at the entry plan of test section are evaluated by means of standard polynomial functions with the reference flow entry temperature T_0 measured at the flow entry plane as the determined variable. An on-line checking procedure is constantly performed during experiments to calculate the fluid temperature rises through the heated channel based on the net amount of convective heating power and the total coolant mass flow rate. Calculated fluid temperature rises between the flow entrance and exit are compared with actual measurements to check the accuracy of energy accountancy. Data batches are only collected when differences between the calculated and measured fluid temperature rises are less than $\pm 10\%$. Local fluid bulk temperatures (T_f) at the streamwise locations corresponding to five measured cross-sectioned planes are calculated using the enthalpy balance method.

2.3. Program

Experimental programs involve three phases. The first phase performs heat transfer experiments in the static curved channel that generates the database against which the reciprocating results obtained at the second phase are compared to highlight reciprocating effects on heat transfer. Angular (θ-wise) Nu variations corresponding to rib-top and mid-rib spots on the inner and outer walls of the curved channel at five streamwise (circumferential) sectional planes with and without system reciprocation are collected for the subsequent parametric analysis. This parametric study, aimed at revealing individual and interactive heat transfer impacts of inertial and reciprocating forces with and without buoyancy interactions, is performed with the addition of a set of zero-buoyancy heat transfer data. In the third phase, a methodology is proposed to devise the physically consistent heat transfer correlation for this particular test channel, which method is applicable to attack different reciprocating flow problems with a variety of geometrical configurations. Experimentally defined local Nusselt numbers (Nu) follow Eq. (2)

$$Nu = qd/k_f(T_w - T_f) \tag{2}$$

The local heat flux to fluids (q) in Eq. (2) is calculated from the heat flux generated in the stainless steel heating foil with a correction to account for external heat losses. Local external heat losses are proportional to the locally prevailing wall-to-ambient temperature differences with various proportionality constants taken from heat loss calibration plots for different locations and reciprocating frequencies. The non-uniform wall-temperature distribution over each rib-roughened heating foil, which reflects the spatial heat transfer variations, creates a corresponding non-uniform distributing pattern of heat loss flux with the larger amounts of external heat loss developed at high temperature spots. This in turn undermines the uniformity of heat flux generated on each heating foil. However, due to the thermal insulation provided by Teflon plates, heat flux distributions on the rib-roughened inner and outer walls are controlled within the maximum variation range of $\pm 6.3\%$, which allows for the approximation of basic uniform heat flux boundary condition. Having acquired the convective heat flux at each measured streamwise (circumferential) sectional plane, fluid bulk temperatures (T_f) in Eq. (2) are calculated based on the concept of enthalpy balance using the sequential integration method from the measured flow entry temperature. Coolant's local properties are accordingly evaluated to account for the influences of T_f variation on physical properties. The characteristic length selected to define Nusselt (Nu), Reynolds (Re), Dean (Dn), pulsating (Pu) and reciprocating Grashof (Gr_p) numbers is the hydraulic diameter of test duct, d.

At each predefined flow condition with specified Re, Dn and Pu values, five heating powers raise wall temperatures at the inner-wall rib-top spot of exit plane to levels of 323, 333, 353,

373 and 393 K. Each set of heat transfer data generated with five different buoyancy levels reveals the individual buoyancy effects on heat transfer. Heat transfer tests are performed with five reciprocating frequencies, namely 0, 0.83, 1.25, 1.67 and 2 Hz at each set of tests organized by five ascending buoyancy levels with a predefined *Re* (*Dn*) number. Five *Re* (*Dn*) numbers of 5000 (1890), 10 000 (3824), 15 000 (5772), 20 000 (7581) and 24 000 (9159) are specified for each set of static and reciprocating tests with five buoyancy levels. For each individual heat transfer test, the flow and heating level are fixed for about 30–45 minutes in order to assure that the flow reaches an equilibrium state. When the time-averaged T_w differences between several successive scans always remain within ±0.5 K, the flow condition is referred to as the temporal-repeated-state. The on-line data acquisition system is then activated to record the instantaneous T_w data for a period of 10 seconds. This set of raw experimental data is subsequently processed to generate the corresponding *Nu*, *Re*, *Dn*, *Pu* and Gr_p; and the individual effect of these parameters on heat transfer examined. Test conditions of these dimensionless parameters are summarized in Table 1. An uncertainty approximation of the data reduction is conducted based on the policy specified by Editorial Board of ASME J. Heat Transfer [25]. Temperature measurements form major sources that attribute to uncertainties for the dimensionless parameters. With the wall-to-fluid temperature differences in the test range of 28 to 102 K, maximum uncertainties for *Nu*, *Re*, *Dn*, *Pu*, and Gr_p were about 13.6%, 4.9%, 5.1%, 2.3% and 5.2%, respectively.

Table 1
Test conditions of experimental dimensionless parameters

Non-dimensional parameter	Test conditions
Reynolds number [*Re*]	5000, 10 000, 15 000, 20 000, 24 000
Dean number [*Dn*]	1890, 3824, 5772, 7851, 9159
Pulsating number [*Pu*]	0–0.07
Pulsating Grashof number [Gr_p]	0–98 500
Prandtl number [*Pr*]	0.69–0.71

3. Results and discussion

3.1. Static results

Nusselt number variations along two opposite inner and outer walls at five sectional planes of $\Phi = 0, 1/4\pi, 1/2\pi, 3/4\pi$ and π in the rib-roughened static duct with Reynolds (Dean) numbers of 10 000 (3824), 15 000 (5772) and 24 000 (9159) are

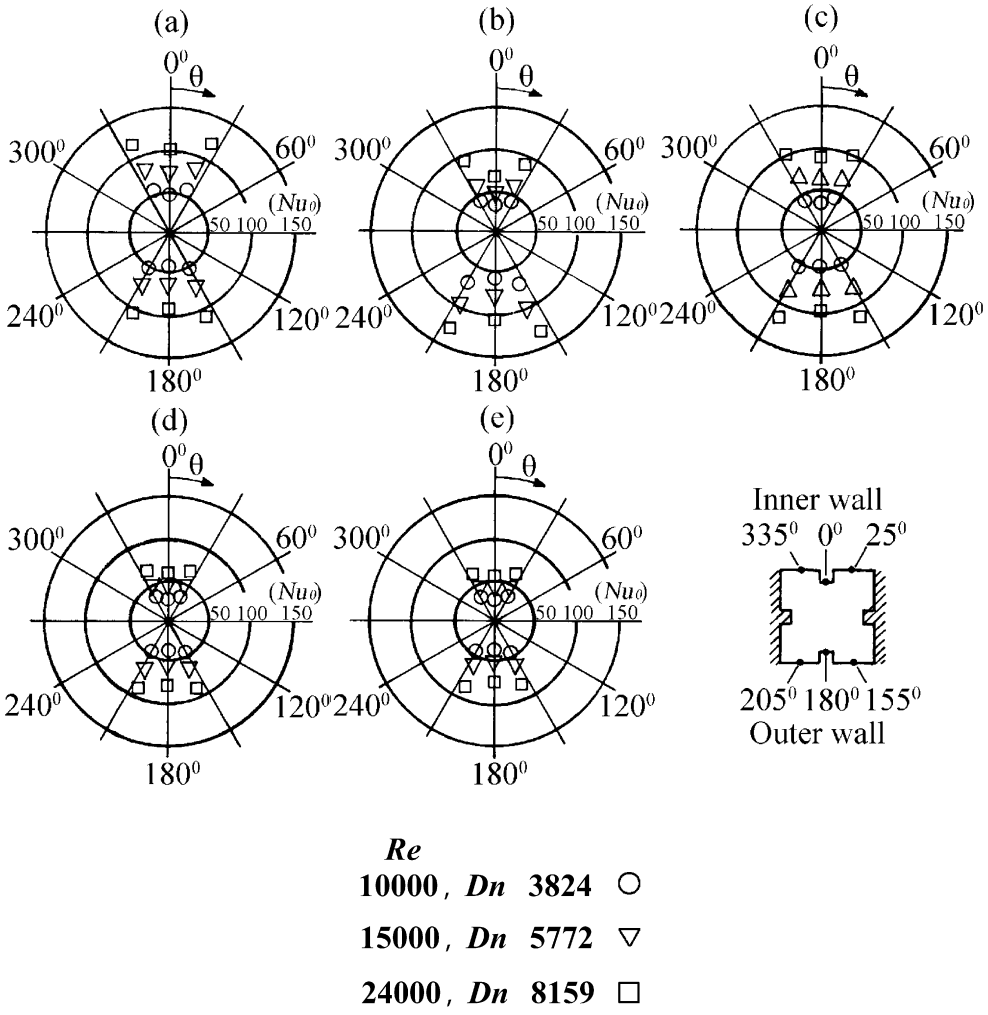

Fig. 3. Angular Nusselt number variations in static curved duct at (a) $\Phi = 0$, (b) $\Phi = \pi/4$, (c) $\Phi = \pi/2$, (d) $\Phi = 3\pi/4$, (e) $\Phi = \pi$.

depicted in Fig. 3. Streamwise developments of Dean vortices in this curved duct are reflected by heat transfer differences between inner and outer walls. At the sectional plane of $\Phi = 0$ where centrifugal forces in the curved duct are initiated, heat transfer differences between outer and inner walls are almost indistinguishable. Large outer-to-inner heat transfer differences develop at the sectional plane of $\Phi = 1/4\pi$ and $1/2\pi$ for all the Reynolds (Dean) numbers tested. Dean vortices at sectional planes of $\Phi = 1/4\pi$ and $1/2\pi$ thus possess the higher strengths. Further downstream of $\Phi = 1/2\pi$, the outer-to-inner heat transfer differences start fading that indicates the weakened Dean secondary flows. At the exit plane of $\Phi = \pi$ where the curvature of test duct terminates, outer-to-inner heat transfer differences still remain weakly as Dean vortices are not yet vanished. As there is no repeated peripheral heat transfer profile observed at these five sectional planes depicted in Fig. 3, the developing nature of Dean vortices in this rib-roughened curve duct is demonstrated. At sectional planes of $\Phi \geqslant 1/4\pi$, increases of *Dn* from 3824 to 9159 augment Dean vortices that incur corresponding increases of outer-to-inner heat transfer differences.

As described previously, the presence of longitudinal ribs in a curved duct disturbs Dean vortices that consequently affects *Dn* impacts on local heat transfer from the smooth-walled scenario. Along with the development of Dean vortices in this curved duct, each longitudinal rib trips Dean vortices that causes the cross-plane secondary flows to separate into small-scaled vortical cells scattering around the longitudinal rib [26]. As a result, local Nusselt numbers at mid-rib spots on both inner and outer walls are consistently higher than that on the rib-top as seen in Fig. 3. Such mid-rib heat transfer enhancement is attributed to the improved fluid mixing motivated by small-scaled vortical flow cells adjacent to each longitudinal rib. Either by increasing *Dn* to strengthen Dean vortices or allocating flow fields at the sectional plane of $\Phi = 1/4\pi$ or $1/2\pi$ where the Dean vortices possess the stronger strengths, a systematic increase of Nu_0 differences between rib-top and its neighboring mid-rib locations is accordingly followed as shown in Fig. 3. A better illustration of this heat transfer phenomenon that features rib-top to mid-rib Nu_0 differences is provided by Fig. 4 in which the streamwise variations of local Nu_0 data collected from each angular (θ) location at *Re* (*Dn*) = 10 000 (3824) and 24 000 (9159) are compared.

As typified in Fig. 4, two sets of data cluster that respectively group Nu_0 data at $\theta = 25°$, 335°, 155°, 205° for mid-rib locations and at $\theta = 0°$, 180° for rib tops are found at $\Phi = 0$ section for each *Re* (*Dn*) number tested. At this $\Phi = 0$ section where Dean vortices are not developed yet, θ-wise Nu_0 variations are produced by longitudinal ribs. Centrifugal forces develop in downstream flows after $\Phi = 0$ section so that two sets of data series that distinguish heat transfers on inner and outer walls are observed at the remaining sectional planes as shown in Fig. 4. Cool core-fluids are convected to the outer wall by centrifugal forces that wash this heated surface and then flow along two side-walls toward the rip-top on the inner wall. As a result, the outer wall consistently operates at the lower temperatures relative to the inner-wall under a basically uniform

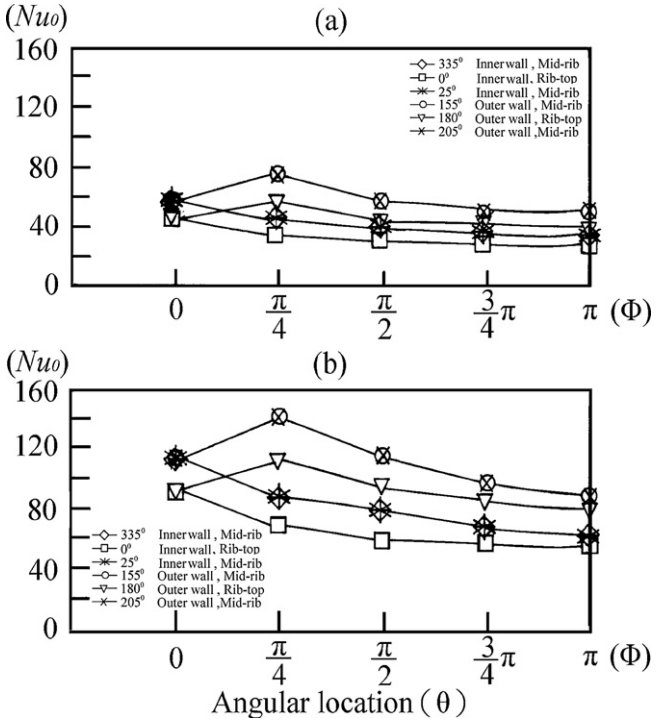

Fig. 4. Streamwise Nusselt number variations in static curved duct at (a) *Re* (*Dn*) = 10 000 (3824), (b) *Re* (*Dn*) = 24 000 (9159).

heat flux condition. Due to this washing effect driven by Dean vortices, Nu_0 levels on the inner wall consistently decrease in the downstream direction from $\Phi = 0$ plane as demonstrated in Fig. 4. At $\Phi = 1/4\pi$ section, Nu_0 levels increase considerably but a streamwise Nu_0 decay is followed after $\Phi = 1/4\pi$ sectional plane. The peak heat transfer levels developed at the outer wall of $\Phi = 1/4\pi$ sectional plane could reflect the synergetic influences of developing rib-flows and Dean-vortices on heat transfer. On either the inner or outer wall in this curved duct, two mid-rib Nu_0 data collapses into a tight band. These two mid-rib Nu_0 levels are higher than that on its neighboring rib-top. As illustrated previously, the presence of longitudinal ribs promotes the development of small-scaled vortical flows in a curved duct that augment local heat transfers in mid-rib regions.

Although interactive influences of longitudinal ribs and centrifugal forces on *local* heat transfers as demonstrated in Figs. 3 and 4 are scientifically merited, the evaluation of overall heat transfer performances for a piston cooling network plays an important role to prevent overheating in the design stage. To quantify the overall cooling performance at each sectional plane of this rib-roughened curve duct, six Nu_0 measurements collected from inner and outer walls at each Φ plane are averaged to acquire the averaged Nusselt number ($\overline{Nu_0}$) for each sectional plane. Fig. 5 depicts the variation of $\overline{Nu_0}$ against *Re* at five sectional planes of $\Phi = 0$, $1/4\pi$, $1/2\pi$, $3/4\pi$ and π. Circumferentially averaged Nusselt number for the smooth-walled curve tube ($\overline{Nu}_0^{SW}$) [3] and Dittus–Boelter Nusselt number (Nu_∞) [27] are also compared in Fig. 5 to highlight the effectiveness of longitudinal ribs on overall heat transfer augmentations. It is noticed that the two pairs of longitudinal ribs

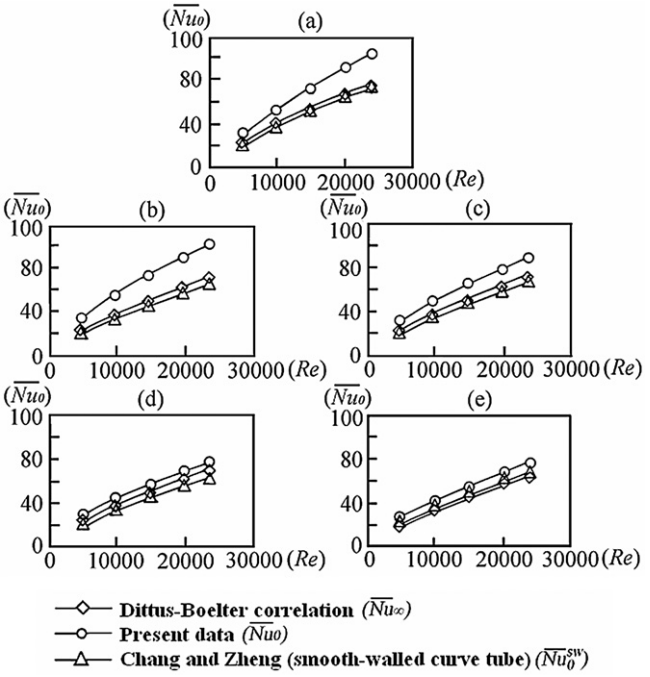

Fig. 5. Variations of averaged heat transfer with Reynolds number at (a) $\Phi = 0$, (b) $\Phi = \pi/4$, (c) $\Phi = \pi/2$, (d) $\Phi = 3\pi/4$, (e) $\Phi = \pi$.

in the straight duct with a $10d$ length prior to the sectional plane of $\Phi = 0$ has augmented heat transfer from the smooth-walled tube level before the coolant entering the curved section. This is indicated by the heat transfer results compared in Fig. 5(a) at $\Phi = 0$ plane. At this $\Phi = 0$ plane, $\overline{Nu}_0^{SW}$ and Nu_∞ are in close agreements but are consistently lower than $\overline{Nu_0}$ for all the Re tested. At $\Phi = 1/4\pi$ section, $\overline{Nu_0}$ values in this rib-roughened curve duct are further enhanced from $\overline{Nu}_0^{SW}$ due to the small-scaled flow cells triggered by longitudinal ribs. Dean vortices in rib-roughened and smooth-walled curve channels have caused $\overline{Nu_0}$ and $\overline{Nu}_0^{SW}$ to be higher than Dittus–Boelter levels (Nu_∞) at $\Phi = 1/4\pi$ section. A streamwise moderation of Dean vortices after $\Phi = 1/4\pi$ plane, which has been unraveled in Fig. 4, undermines the downstream heat transfer augmentations. At the sectional plane of $\Phi = 1/2\pi$, the degrees of heat transfer augmentation in the ribbed curve channel relative to the smooth-walled tube are moderated while the comparative differences of $\overline{Nu_0} > \overline{Nu}_0^{SW} > Nu_\infty$ still follow the result found at $\Phi = 1/4\pi$ section. At $\Phi = 3/4\pi$ and π, heat transfer augmentations induced by ribs or centrifugal forces are very weak as indicated by Figs. 5(d) and 5(e). A review of entire $\overline{Nu_0}$ measurements collected from all Φ sections reveals that the augmented Nusselt numbers in the static rib-roughened curve duct fall in the range of 1.2–1.45 times of the Nusselt numbers in smooth-walled curve tube.

In the static curved duct fitted with longitudinal ribs, heat transfer measurements acquired from five variable heat fluxes for all Re (Dn) numbers tested collapse into a tight data band at each streamwise and angular locations. The impact of gravitation-driven buoyancy on heat transfer in the static rib-roughened duct within the Gr range of 7500–45 000 remains negligible. As there is neither the noticeable change in Pr of coolant nor the considerable buoyancy interaction in the static duct, data trends depicted in Fig. 5 enable the $\overline{Nu_0}$ correlation to be formatted as Eq. (3).

Table 2
Coefficients A and B for static curved duct fitted with longitudinal ribs

Streamwise location X (x/d)	Radian of curvature Φ (rad)	$\overline{Nu_0} = A(\Phi)\,Re^{B(\Phi)}$	
		A	B
10	0	0.031	0.81
14.8	$\pi/4$	0.045	0.78
19.7	$\pi/2$	0.046	0.75
24.4	$3\pi/4$	0.054	0.73
29.6	π	0.069	0.70

$$\overline{Nu_0} = A(\Phi)\,Re^{B(\Phi)} \tag{3}$$

Coefficients A and B in Eq. (3) are functions of streamwise location. Eq. (3) satisfies the limiting condition of zero coolant mass flow with $\overline{Nu_0} = 0$ as $Re = 0$ that features the vanished forced convective capability in the static curved duct. Table 2 summarizes the correlating coefficients A and B at various streamwise (Φ) locations.

As displayed in Table 2, variations of coefficients A and B reflect the varying manner of heat transfer in the streamwise direction that reconfirm the developing nature of Dean vortices. The streamwise increase of A value suggests the enhancing influences of Dean vortices on heat transfer along the curved channel. The streamwise reduction of B value from 0.8 at $\Phi = 0$ plane to 0.7 at $\Phi = \pi$ plane indicates the weakened forced convective inertial effect on heat transfer due to the development of Dean vortices. Over the entire Re (Dn) range tested for all the heat flux levels examined, 95% of experimental $\overline{Nu_0}$ values are correlated by Eq. (3) within $\pm 10\%$ discrepancies. As Pr effects on $\overline{Nu_0}$ are absorbed into correlating coefficients in Eq. (3), the static results of this study are essentially limited to dry air. Having established the non-reciprocating heat transfer references quantified by Eq. (3), comparative heat-transfer differences between static and reciprocating curved ducts are assessable.

3.2. Reciprocating results

Reciprocating forces arise in the direction orthogonal to centrifugal forces when the curved duct reciprocates that modify the static heat transfer phenomena. Such cyclic reciprocating body forces trigger temporal variations of vortical flow cells induced by longitudinal ribs and centrifugal forces with attendant temporal heat transfer variations. The present study generates time-averaged heat transfer results along six angular edges of the rib-roughened curve duct by taking the averaged data of time-wise local Nusselt numbers for a period of 10 seconds. Fig. 6 depicts the θ-wise Nu distributions on two opposite inner and outer walls at five sectioned planes of $\Phi = 0$, $\pi/4$, $\pi/2$, $3\pi/4$, and π. This set of Nu data is generated at the nominal Re (Dn) number of 15 000 (5772) with four pulsating numbers (Pu) of 0, 0.009, 0.018 and 0.021. Reciprocating Grashof number (Gr_p) for all the data collected in Fig. 6 is selected

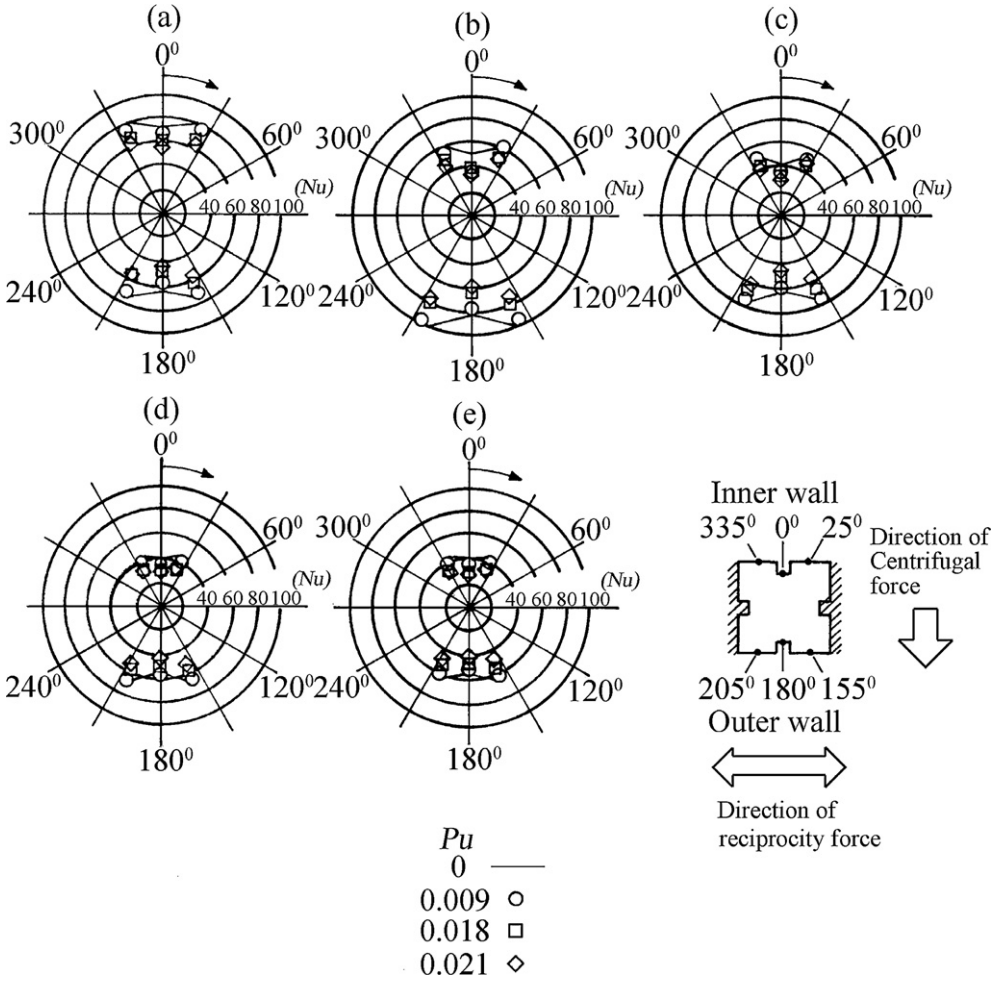

Fig. 6. Angular variations of Nusselt number in reciprocating duct with Re (Dn) = 15 000 (5772), Gr_p = 13 800, Pu = 0, 0.009, 0.018 and 0.021 at (a) $\Phi = 0$, (b) $\Phi = \pi/4$, (c) $\Phi = \pi/2$, (d) $\Phi = 3\pi/4$, (e) $\Phi = \pi$.

at a nominal value of 13 800. As reciprocating forces are orthogonal to centrifugal forces that point toward two side edges of $\theta = 90°$ and 270°, θ-wise Nu distributions are symmetrical about the angular plane connecting inner ($\theta = 0°$) and outer ($\theta = 180°$) edges. The higher Nu levels still develop on mid-rib locations relative to that on their neighboring rib-top as depicted in Fig. 6. Local reciprocating Nu values on outer wall are consistently higher than the counterparts on inner-wall over the sectional planes of $\Phi = \pi/4$, $\pi/2$, $3\pi/4$, and π. Centrifugal-force induced Dean vortices also persist in mainstream even if reciprocating forces prevail over the entire flow domain. These time averaged heat transfer results in the reciprocating duct showed in Fig. 6 follow the characteristics found in the static duct as seen in Fig. 3. But the presence of reciprocating forces with relative strengths controlled in the range of $0 < Pu \leqslant 0.021$ impairs local heat transfer from the static reference. As indicated in each plot of Fig. 6, the increase of pulsating number from 0 to 0.021 at Re (Dn) of 15 000 (5772) induces a systematic heat transfer reduction from the static level at each angular (θ) location. Heat transfer characteristics typified in Fig. 6 are shared by all the reciprocating test results that are subjects of combined Re (Dn)–Pu effects at a selected Gr_p. Although the secondary flows induced by centrifugal forces and longitudinal ribs in the reciprocating duct undergo temporal variations, the time-mean secondary flow structures are likely to follow those developed in the static duct. This is justified by the similar data trends in the respects of outer-to-inner and mid-rib to rib-top Nu differences for both static and reciprocating results. Fluid mechanisms that cause heat transfer reduction from the static reference in the present Re (Dn) and Pu ranges shall follow those found in the ducts with spanwise wall oscillations [22–24]. For the ducted flows with wall oscillations [22–24], the thickened boundary layers along with weakened turbulence intensities are attributed to the reduction of turbulent drag that could also cause heat transfer reductions.

Impacts of reciprocating buoyancy on heat transfer are observed in present test channel. This is demonstrated by Fig. 7 in which three sets of angular Nu variations with three ascending buoyancy levels at Re (Dn) and Pu of 5000 (1890) and 0.027 are compared. Increases of Gr_p value produce a corresponding increase of local Nu level at each sectional plane that reflects the improving buoyancy effect on heat transfer. In this particular Gr_p range tested, the larger data-bands driven by varying buoyancy level develop on the outer wall relative to its inner counterpart as indicated in Fig. 7. A higher degree of buoyancy impact on heat transfer in this reciprocating duct develops

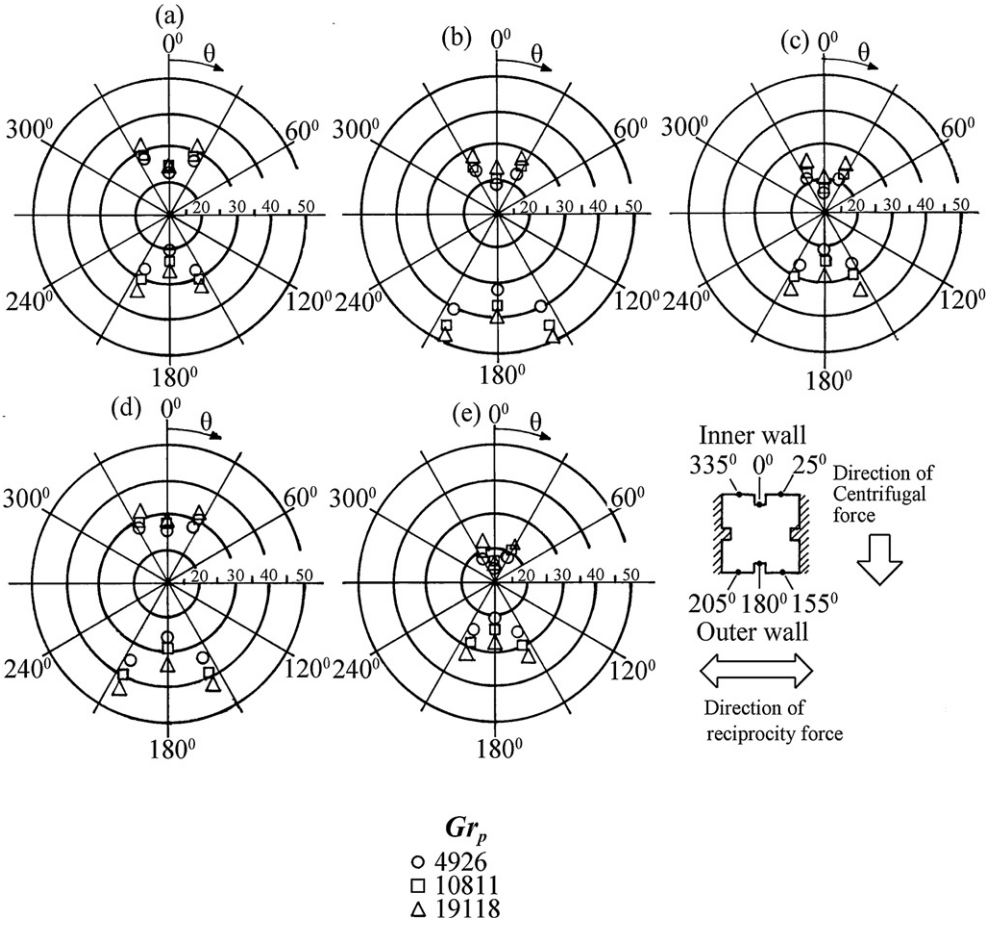

Fig. 7. Influences of Gr_p on local heat transfer in reciprocating duct with Re (Dn) = 5000 (1890) and $Pu = 0.027$ at (a) $\Phi = 0$, (b) $\Phi = \pi/4$, (c) $\Phi = \pi/2$, (d) $\Phi = 3\pi/4$, (e) $\Phi = \pi$.

on the outer wall at each sectional plane examined. Although the buoyancy effect in isolation is shown to improve local heat transfer that is consistently identified within the entire parametric ranges tested, degrees of buoyancy effect on heat transfer are location and Pu dependent. The parametric presentation of reciprocating heat transfer data provides a better illustration for such interactive Pu–Gr_p effects which is described in the following section.

To highlight the coupling Re (Dn)–Pu impact on heat transfer at a specific buoyancy level, each heat transfer measurement is converted into Nusselt number ratio that is obtained by normalizing the reciprocating Nusselt number (Nu) with the equivalent static Nusselt number (Nu_0) obtained at the same Re (Dn) number. Ratios of Nu/Nu_0 quantify the combined Re (Dn)–Pu–Gr_p impacts on heat transfer. As an illustrative example, heat transfer measurements collected in Fig. 6 are converted into Nusselt number ratios (Nu/Nu_0) as depicted in Fig. 8. A consistent data trend of heat transfer reduction in corresponding to the increase of Pu is demonstrated by Fig. 8. For this set of test conditions, the most considerable heat transfer reductions develop at the outer edge ($\theta = 180°$) on two sectional planes of $\Phi = 3\pi/4$ and π at which the Nu/Nu_0 ratios are reduced to the values about 0.75 at the pulsating number of 0.021. Ratios of Nu/Nu_0 at rib-top locations are slightly lower than their neighboring mid-rib spots on both inner and outer walls as shown in Fig. 8. This indicates a further heat transfer reduction at the rib-top relative to its neighboring mid-rib locations due to reciprocating force effects. Differences in Nu/Nu_0 ratios between two opposite inner and outer walls are very small. Influences of reciprocating forces on heat transfer over inner and outer walls thus share the similar degrees of impact. As illustrated previously, the flow structures developed in the static duct remain in the reciprocating duct so that the symmetrical profiles of Nu/Nu_0 in respect to the plane connecting inner and outer edges are retained. Heat transfer characteristics unraveled by Fig. 8 typify all the reciprocating test results. However, Nu/Nu_0 ratios for isothermal flows in this reciprocating duct are further reduced as the improving buoyancy effect on heat transfer is absent. This set of zero-buoyancy heat transfer data is generated by extrapolating Nu/Nu_0 measurements toward the asymptotic conditions of $Gr_p = 0$. Section 3.3 that deals with the development of heat transfer correlation provides a detailed illustration for this extrapolating procedure.

Heat transfer performances collected from present test duct and various reciprocating channels [3,8,9] with specific ranges of parametric conditions are compared in Table 3. The helical tube fitted with full circumferential ribs [9] provides the highest Nu_0 levels among the comparative groups summarized in Table 3. Ratios of Nu/Nu_0 fall in the range of 0.7–1.3 for the enhanced reciprocating channels [8,9]. The most considerable

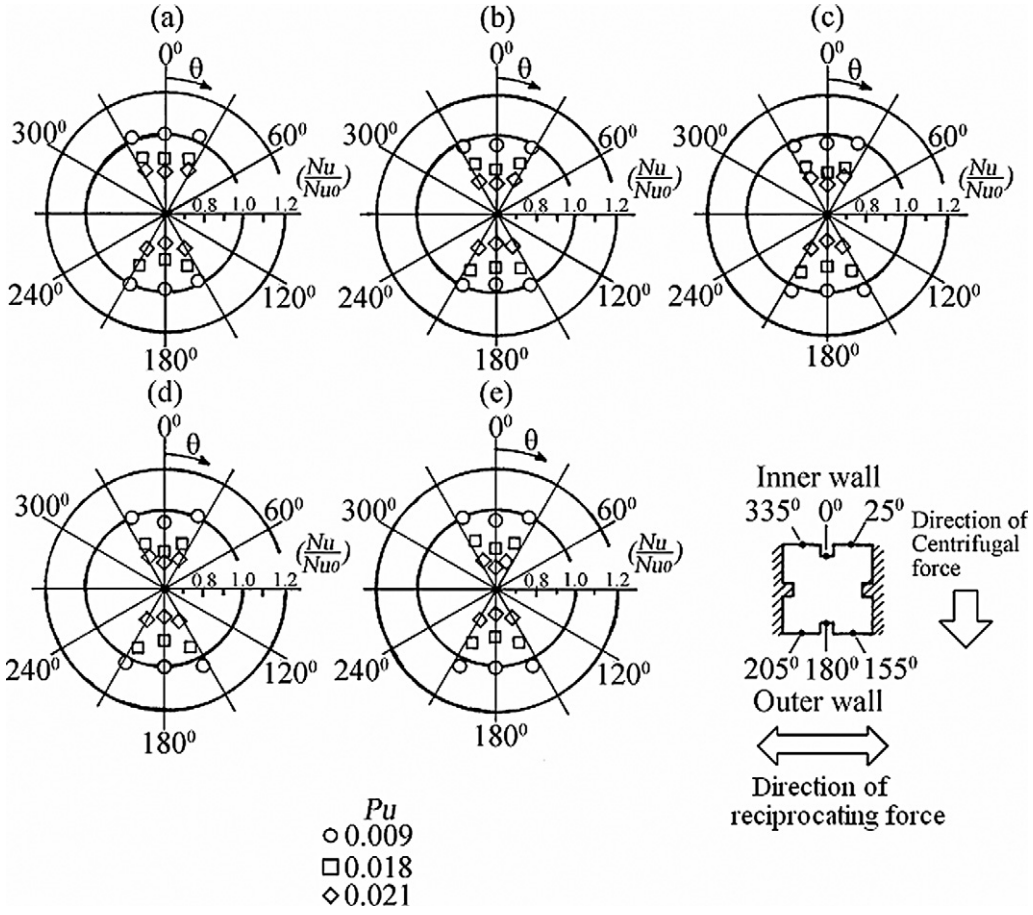

Fig. 8. Angular variations of Nu/Nu_0 ratio in reciprocating duct with Re $(Dn) = 15\,000$ (5772), $Gr_p = 13\,800$, $Pu = 0$, 0.009, 0.018 and 0.021 at (a) $\Phi = 0$, (b) $\Phi = \pi/4$, (c) $\Phi = \pi/2$, (d) $\Phi = 3\pi/4$, (e) $\Phi = \pi$.

Table 3
Reciprocating heat transfer performances for various channel configurations

Reciprocating test configuration	Re	Pu	Gr_p	Nu_0	Nu/Nu_0
Present curved duct with longitudinal ribs	5000–24 000	0–0.07	0–985 000	31–92	0.76–1.25
Curved tube with smooth wall [3]	2500–14 500	0–0.55	0–970 000	25–50	0.60–1.15
Straight tube with twisted-tape [8]	3000–12 000	0–0.9	0–976 000	23–98	0.70–1.30
Helical tube with full circumferential ribs [9]	4500–7000	0–0.4	0–981 000	30–90	0.71–1.21

heat transfer impediments due to channel reciprocation develop in the curved tube with smooth wall [3]. About 40% of heat transfer reduction from the static Nusselt number level (Nu_0) could take place in the reciprocating curved tube with smooth wall [3]. With the longitudinal ribs attached in the reciprocating curved duct, the severe heat transfer reductions developed in the smooth-walled curve tube [3] are recovered to the levels about 34%. Heat transfer improvements from the static scenarios at the high pulsating numbers for the reciprocating planner curved channels are also raised from 1.12 [3] to 1.25. In the respect of heat transfer performances for reciprocating planner curve channels, the advantages of fitting longitudinal ribs are demonstrated.

3.3. Heat transfer correlation

Designs of an internally cooled piston require the evaluation of overall cooling capability for its internal cooling network. The overall convective capability in terms of $\overline{Nu}/\overline{Nu_0}$ at each sectional plane of this reciprocating rib-roughened curve duct is determined by averaging six Nu/Nu_0 measurements collected from two opposite inner and outer walls at each sectional plane. Based on the experimental evidences described previously, the averaged Nusselt number ratio ($\overline{Nu}/\overline{Nu_0}$) is parametrically controlled by Re (Dn), Pu and Gr_p. The variation ranges of $\overline{Nu}/\overline{Nu_0}$ ratios for each set of parametric conditions tested are summarized in Table 4. The range of $\overline{Nu}/\overline{Nu_0}$ ratio for each specified Re (Dn) and Pu numbers in Table 4 is produced by varying the Gr_p values. At each controlled Re (Dn) number indicated in Table 4, about 20% of $\overline{Nu}/\overline{Nu_0}$ variations are produced within the present Gr_p range. Heat transfer impediments due to channel reciprocation are gradually recovered as Re (Dn) increases. The interactive Re (Dn)–Pu–Gr_p effects on heat transfer are implicitly indicated in the data pool summarized in Table 4.

It is worth noting that $\overline{Nu}/\overline{Nu_0}$ measurements generated by heat transfer experiments inevitably inherit certain degrees of buoyancy interaction as finite wall-to-fluids temperature differences are required to define heat transfer coefficients. Therefore the usage of direct heat transfer measurements to identify

Table 4
Ranges of Nu/Nu_0 at various parametric conditions

Re (*Dn*)	*Pu*	0.027	0.041	0.054	0.065
5000 (1890)	$\overline{Nu}/\overline{Nu_0}$	0.83–1.12	0.74–0.98	0.63–0.82	0.66–0.86
Re (*Dn*)	*Pu*	0.014	0.020	0.027	0.033
10 000 (3824)	$\overline{Nu}/\overline{Nu_0}$	0.87–1.03	0.85–1.03	0.70–0.82	0.69–0.88
Re (*Dn*)	*Pu*	0.009	0.013	0.018	0.022
15 000 (5772)	$\overline{Nu}/\overline{Nu_0}$	0.93–1.01	0.91–1.01	0.74–0.89	0.72–0.84
Re (*Dn*)	*Pu*	0.007	0.011	0.014	0.016
20 000 (7851)	$\overline{Nu}/\overline{Nu_0}$	0.98–1.04	0.97–1.03	0.78–0.86	0.73–0.80
Re (*Dn*)	*Pu*	0.006	0.008	0.011	0.014
24 000 (9159)	$\overline{Nu}/\overline{Nu_0}$	0.98–1.08	0.94–1.06	0.83–0.91	0.83–0.94

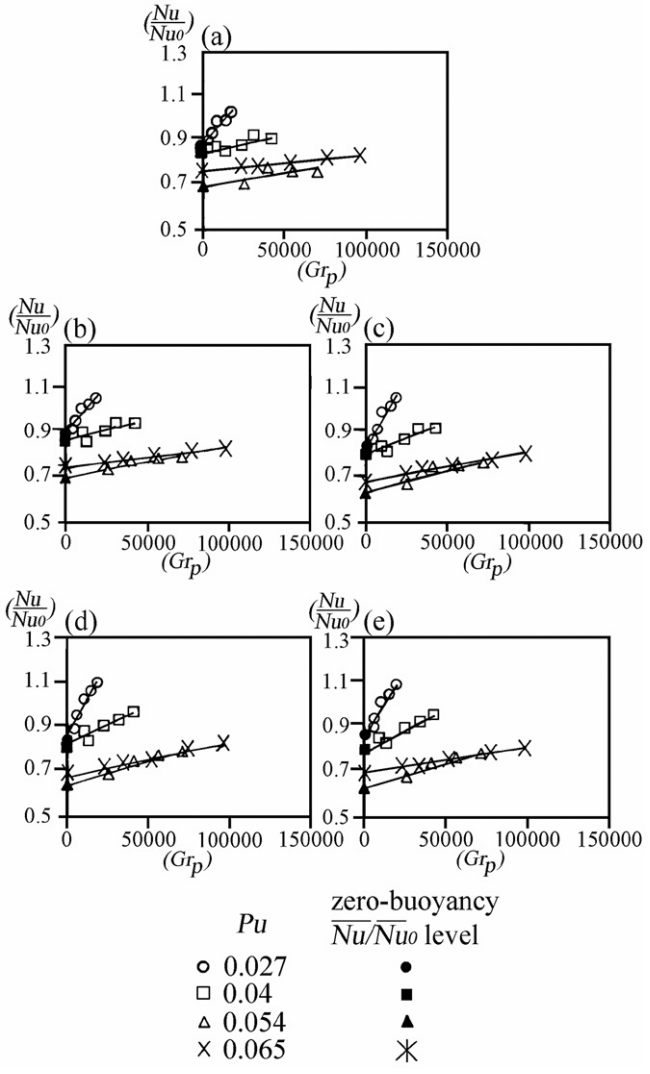

Fig. 9. Variations of averaged heat transfer with Gr_p at (a) $\Phi = 0$, (b) $\Phi = \pi/4$, (c) $\Phi = \pi/2$, (d) $\Phi = 3\pi/4$, (e) $\Phi = \pi$.

Re (*Dn*)–*Pu* impacts on heat transfer without any buoyancy interaction is not practical. The attempt to unravel the so-called zero-buoyancy heat transfer data is performed by extrapolating a set of data series organized by five $\overline{Nu}/\overline{Nu_0}$ measurements obtained with five different Gr_p values onto the asymptotic limit of zero Gr_p condition. Each five-point $\overline{Nu}/\overline{Nu_0}$ series at a particular set of *Re* (*Dn*) and *Pu* numbers are plotted against Gr_p as shown in Fig. 9 to demonstrate such data extrapolating process.

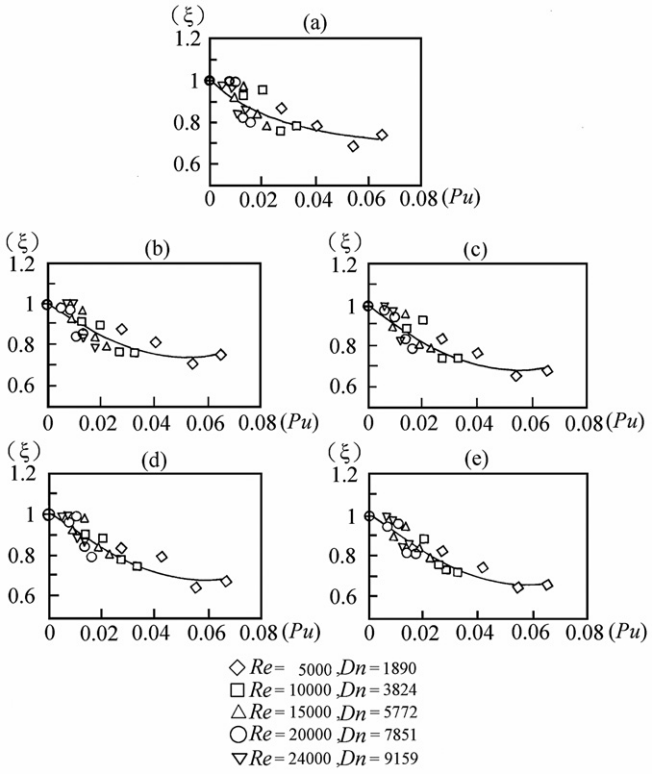

Fig. 10. Variations of zero buoyancy heat transfer level with *Pu* at (a) $\Phi = 0$, (b) $\Phi = \pi/4$, (c) $\Phi = \pi/2$, (d) $\Phi = 3\pi/4$, (e) $\Phi = \pi$.

At each set of *Re* (*Dn*) and *Pu* numbers, $\overline{Nu}/\overline{Nu_0}$ ratios increase linearly as Gr_p increases for each five-point data series that is consistently followed by all the data series collected in Fig. 9. This result reconfirms that the reciprocating buoyancy effect improves heat transfer for present parametric conditions examined. However, slopes of these five-point $\overline{Nu}/\overline{Nu_0}$ data trends at any sectional plane showed in Fig. 9 decrease as *Pu* increases. The weakened buoyancy effect on heat transfer as *Pu* increases is observed so that the interactive Gr_p–*Pu* influences on reciprocating heat transfer are confirmed. The extrapolation of each data series onto its limiting condition of $Gr_p = 0$ acquires the zero-buoyancy $\overline{Nu}/\overline{Nu_0}$ ratio at the corresponding set of *Re* (*Dn*) and *Pu* numbers. Nusselt number ratios ($\overline{Nu}/\overline{Nu_0}$) at $Gr_p = 0$ is treated as an additional set of heat transfer data with vanished buoyancy interaction. The data trends depicted in Fig. 9 along with the extrapolated zero-buoyancy $\overline{Nu}/\overline{Nu_0}$ data are approximated by the liner version of heat transfer correlation taking the form of Eq. (4). ξ and ζ functions in Eq. (4) respectively quote for the zero-buoyancy $\overline{Nu}/\overline{Nu_0}$ data and the slope of each data trend shown in Fig. 9 that is *Pu* and *Re* (*Dn*) dependent.

$$\overline{Nu}/\overline{Nu_0} = \xi\{Pu, Re\} + \zeta\{Pu, Re\}Gr_p \tag{4}$$

Variations of zero-buoyancy $\overline{Nu}/\overline{Nu_0}$ ratios (ξ values) against *Pu* with five sets of *Re* (*Dn*) numbers at five sectional planes are summarized in Fig. 10. $\overline{Nu}/\overline{Nu_0}$ ratios at each sectional plane shown in Fig. 10 are continuously reduced from unity as *Pu* increases from 0 to 0.07. At the limiting condition of zero reciprocation, $\overline{Nu}/\overline{Nu_0}$ ratios become unity to recover sta-

Table 5
Coefficients f_a and f_b in Eq. (5)

Streamwise location X (x/d)	Radian of curvature Φ (rad)	$\xi = 1 + f_a(\Phi)Pu + f_b(\Phi)Pu^2$	
		f_a	f_b
10	0	−9.25	78.21
14.8	$\pi/4$	−9.72	89.09
19.7	$\pi/2$	−10.29	85.60
24.4	$3\pi/4$	−10.97	91.93
29.6	π	−11.39	93.41

tic heat transfer solutions correlated by Eq. (3). Without the additional heat transfer improvement provided by buoyancy interactions in this reciprocating duct, the *Pu* driven heat transfer impediment shown in Fig. 10 has led $\overline{Nu}/\overline{Nu_0}$ ratios to the levels about 0.7 at the pulsating number of 0.058. The isolated *Pu* effect that impedes heat transfer has to be particularly considered when the rib-roughened curve channel is employed as a part of cooling network in a piston. In each plot of Fig. 10, data points of $\overline{Nu}/\overline{Nu_0}$ ratio obtained with five *Re* (*Dn*) numbers ranging from 5000 (1890) to 24 000 (9150) collapse into a tight data band with a maximum spreading range of 12%. Such data collapsing tendency enables the zero-buoyancy $\overline{Nu}/\overline{Nu_0}$ data to be correlated into a *Pu* controlled function. Justified by all the data trends depicted in Fig. 10, $\overline{Nu}/\overline{Nu_0}$ ratios at the zero-buoyancy condition defined as ξ function are correlated into Eq. (5). The limiting condition of zero-reciprocation with $Pu = 0$ forces ξ value into unity in Eq. (5) that recovers the static heat transfer scenarios.

$$\xi = 1 + f_a(\Phi)Pu + f_b(\Phi)Pu^2 \tag{5}$$

Table 5 summarizes the numerically determined curve fits for f_a and f_b coefficients in Eq. (5), which are Φ dependent.

Experimental evidences collected in Fig. 9 formulate Eq. (4) that indices the reciprocating buoyancy impact on heat transfer as ζ value. Inter-correlations between Gr_p and *Pu*, *Re* (*Dn*) in the $\overline{Nu}/\overline{Nu_0}$ correlation exist as ζ values vary with *Pu* and *Re* (*Dn*). Varying manners of ζ value against *Pu* at five *Re* (*Dn*) numbers are revealed in Fig. 11. These ζ values follow an exponential decay as *Pu* increases at each fixed *Re* (*Dn*) number. The variation of ζ value against *Pu* at each *Re* (*Dn*) number behaves on its own right in Fig. 11. The degree of reciprocating buoyancy impact on heat transfer appears to be *Re* (*Dn*) dependent. Increases of *Re* (*Dn*) number systematically drive each *Re* (*Dn*) controlled data trend away from the origin of Fig. 11. A large ζ value for a given *Pu* number thus develops at the flow condition with a higher *Re* (*Dn*) number. A physical interpretation of this result is that the increase of *Re* (*Dn*) number augments reciprocating buoyancy impact on heat transfer. The dependency of ζ value on *Pu* indicates the inter-correlative *Pu*–Gr_p impact on heat transfer. Such interactive *Pu*–Gr_p impacts on heat transfer are *Re* (*Dn*) dependent which leads to an inter-correlative *Pu*–Gr_p–*Re* (*Dn*) complex to define the buoyancy effect on $\overline{Nu}/\overline{Nu_0}$ ratio. Justified by all the data trends depicted in Fig. 11 at five sectional planes, ζ value can be well correlated by the functional structure of

$$\zeta = a_0\{Re, \Phi\} + a_1\{Re, \Phi\}e^{a_2\{Re\ (Dn), \Phi\}Pu} \tag{6}$$

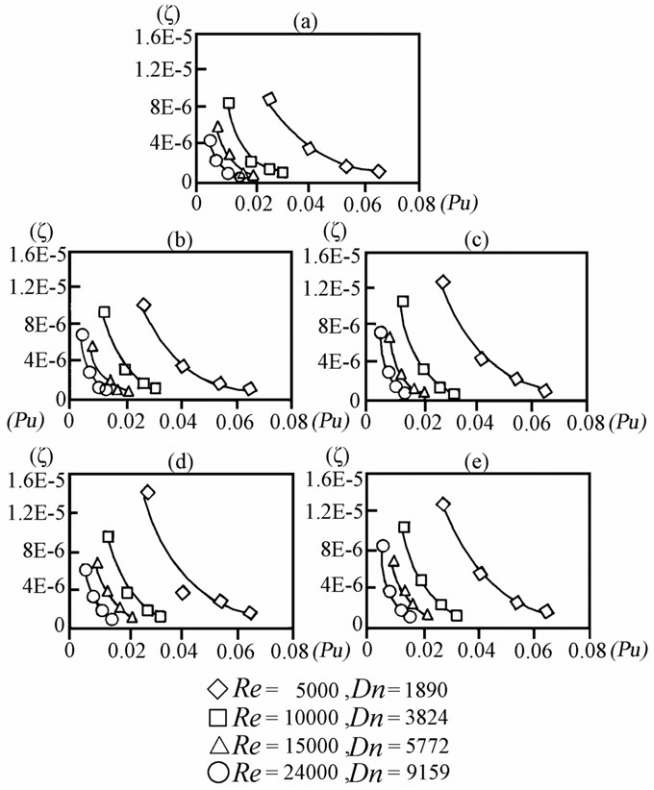

Fig. 11. Variations of buoyancy impact (ζ function) on heat transfer with *Pu* at (a) $\Phi = 0$, (b) $\Phi = \pi/4$, (c) $\Phi = \pi/2$, (d) $\Phi = 3\pi/4$, (e) $\Phi = \pi$.

Coefficients a_0, a_1 and a_2 are functions of *Re* and Φ. It is worth emphasizing that, for a specified curved duct with a selected d/D ratio, *Dn* is evaluated as $Re\sqrt{d/D}$ so that the inter-correlative relationship between *Re* and the coupling *Pu*–Gr_p impact on heat transfer described by a_0, a_1 and a_2 in Eq. (6) implicitly involves *Dn* impact. Fig. 12 shows the varying manners of coefficients a_S against *Re* at five sectional planes. Quadric functions expressed by Eq. (7) are capable of well correlating coefficients a_S into the functions of *Re* as demonstrated in Fig. 12.

$$a_S = a_S^0(\Phi) + a_S^1(\Phi)Re + a_S^2(\Phi)Re^2 \tag{7}$$

Coefficients a_S^0, a_S^1 and a_S^2 in Eq. (7) are Φ dependent as summarized in Table 6.

The net result of this phase of study is an empirical heat transfer correlation of Eq. (4) that evaluates $\overline{Nu}/\overline{Nu_0}$ ratios at five sectional planes examined. The overall success of this heat transfer correlation is demonstrated by Fig. 13 in which the entire experimental $\overline{Nu}/\overline{Nu_0}$ data are compared with the calculated results using Eq. (4). A maximum discrepancy of ±25% between the experimental and correlating results is achieved for 92% of the entire data set generated. The ratios of $\overline{Nu}/\overline{Nu_0}$ for this reciprocating curve duct fitted with two pairs of longitudinal ribs depicted in Fig. 13 are in the range of 0.7–1.3 due to combined *Pu*–*Re* (*Dn*)–Gr_p impacts on heat transfer. In the reciprocating smooth-walled curve tube, $\overline{Nu}/\overline{Nu_0}$ ratios fall in the range of 0.6–1.15 [3]. Despite the fact that the augmented Nusselt numbers in the static rib-roughened curve duct are in the range of 1.2–1.45 times of smooth-walled curve-tube val-

Table 6
Coefficients a_S^0, a_S^1 and a_S^2 five Φ planes

$a_S = a_S^0(\Phi) + a_S^1(\Phi)Re + a_S^2(\Phi)Re^2$					
X	10	14.8	19.7	24.4	29.6
Φ	0	$\pi/4$	$\pi/2$	$3\pi/4$	π
a_0^0	2.933E–7	7.039E–7	1.126E–6	1.204E–6	4.279E–7
a_0^1	6.903E–11	2.419E–11	−2.690E–12	−4.907E–12	6.517E–11
a_0^2	−2.112E–15	−1.294E–15	−6.368E–16	−6.052E–16	−2.276E–15
a_1^0	−2.503E–5	−3.854E–4	−1.747E–4	1.294E–4	−5.041E–6
a_1^1	2.744E–8	1.304E–7	8.386E–8	1.201E–8	2.971E–8
a_1^2	−1.038E–12	−4.598E–12	−2.960E–12	−5.623E–13	−1.126E–12
a_2^0	1.253E–2	2.624E–2	2.362E–2	1.679E–2	1.955E–2
a_2^1	−4.636E–2	−7.624E–2	−6.982E–2	−5.221E–2	−5.734E–2
a_2^2	9.542E–7	1.689E–6	1.509E–6	1.012E–6	1.310E–6

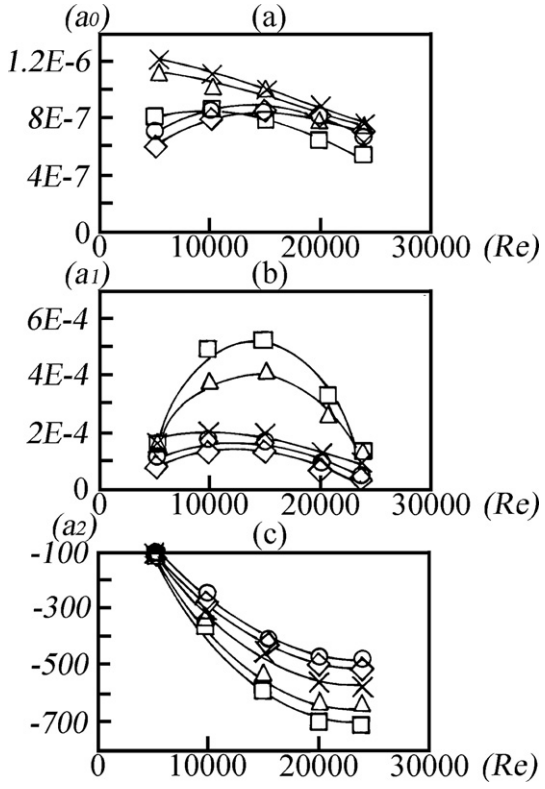

Fig. 12. Variations of a_S coefficients with Reynolds number for (a) a_1, (b) a_2, (c) a_3.

ues as the longitudinal ribs trip the curvature induced vortices that promotes heat transfer, the lower end of $\overline{Nu}/\overline{Nu_0}$ ratios in the present reciprocating rib-roughened curve duct are higher than those found in the reciprocating smooth-walled curve tube. Nevertheless, considerable heat transfer reductions in the reciprocating rib-roughened curve duct within the present *Pu* range examined need particular attentions to avoid the development of overheating spots in a piston. Owing to the complex and interactive *Pu*–*Re* (*Dn*)–Gr_p impacts on the thermal fluids phenomena in this present reciprocating rib-roughened curve channel, it is a formidable task to numerically attack this heat transfer problem. However, based on the accuracy achieved by Eq. (4),

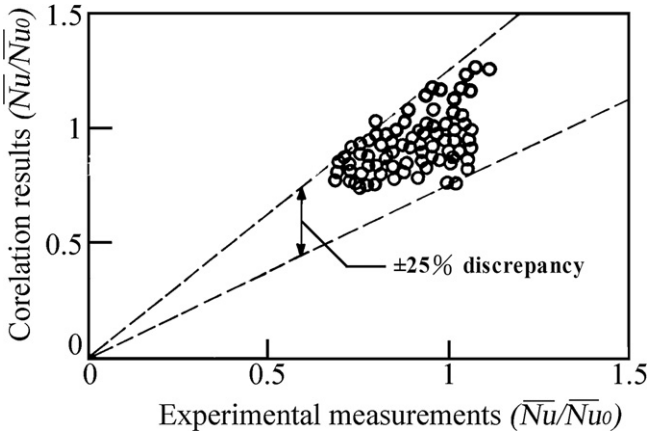

Fig. 13. Comparison of experimental measurements with correlation results.

reasonable heat transfer evaluations for an internal cooling network of piston that employs the present test geometry are attainable in the design phase.

4. Conclusions

This experimental study investigates the convective heat transfer in a reciprocating square-sectioned curve duct fitted with a centerline longitudinal rib on each wall. Justified by the experimental heat transfer results, Dean vortices induced by centrifugal-forces in the curved duct still persist in the mainstream even if reciprocating forces prevail over the entire flow domain. The cyclic reciprocating forces acting in the direction orthogonal to the centrifugal forces trigger temporal variations of vortical flow cells induced by centrifugal forces and longitudinal ribs with the attendant temporal heat transfer variations generated. Illustrations of thermal fluids physics based on the time-averaged heat transfer data reveal individual and interactive influences of centrifugal, pulsating and buoyancy forces on heat transfer in the square-sectioned reciprocating rib-roughened curve duct. Following concluding remarks emerge from this study.

1. Longitudinal ribs trip curvature induced Dean vortices to produce small-scaled vortical flow cells scattering around each longitudinal rib that elevate mid-rib Nu_0 values from the neighboring rib-top levels. Static Nusselt number in this rib-roughened curve duct is in the range of 1.2–1.45 times of that in the smooth-walled curve tube which is correlated by Eq. (3).
2. The isolated *Pu* effect in the parametric range of $0 < Pu < 0.07$ is location dependent that impairs heat transfer in the reciprocating duct. The most considerable heat transfer reductions in the reciprocating rib-roughened curve duct from the static conditions develop at the outer edge ($\theta = 180°$) on two sectional planes of $\Phi = 3\pi/4$ and π. Heat transfers at rib-top location are further reduced form its neighboring mid-rib spots due to reciprocating force effects.
3. Reciprocating buoyancy (Gr_p) effect in isolation improves heat transfer. Degrees of Gr_p impact on heat transfer decreases as *Pu* increases that unravels the Gr_p–*Pu* interactive influence. As the interactive Gr_p–*Pu* effect on heat transfer is augmented as *Re* (*Dn*) increases, an inter-correlative Gr_p–*Pu*–*Re* (*Dn*) complex that defines the reciprocating buoyancy effect on heat transfer is demonstrated.
4. Combined *Pu*–*Re* (*Dn*)–Gr_p impacts have led $\overline{Nu}/\overline{Nu_0}$ ratios in the rib-roughened curve duct to the values in the range of 0.7–1.3. Such interactive *Pu*–*Re* (*Dn*)–Gr_p effects as well as the isolated *Re* (*Dn*), *Pu* and Gr_p impact on heat transfer in this reciprocating rib-roughened curve duct have been taken into account in the physically consistent heat transfer correlation developed for evaluating $\overline{Nu}/\overline{Nu_0}$ ratio.

Acknowledgements

The research facilities are financially supported by National Science Council, Taiwan, Republic of China, under grant number, NSC 91-2611-E-022-003.

References

[1] T.L. Yang, S.W. Chang, L.M. Su, C.C. Hwang, Heat transfer of confined impinging jet onto spherically concave surface with piston cooling application, JSME Int. J. B 42 (2) (1999) 238–248.
[2] S.W. Chang, L.M. Su, W.D. Morris, T.M. Liou, Heat transfer in a smooth-walled reciprocating anti-gravity open thermosyphon, Int. J. Thermal Sci. 42 (2003) 1089–1103.
[3] S.W. Chang, Y. Zheng, Heat transfer in reciprocating planar curved tube with piston cooling application, ASME J. Gas Turbine and Power 128 (2006) 219–229.
[4] G. Fabbri, Optimum profiles for asymmetrical longitudinal fins in cylindrical ducts, Int. J. Heat Mass Transfer 42 (1999) 511–523.
[5] C.V.M. Braga, F.E.M. Saboya, Turbulent heat transfer, pressure drop and fin efficiency in annular regions with continuous longitudinal rectangular fins, Exp. Thermal Fluid Sci. 20 (1999) 55–65.
[6] İ. Dağtekin, H.F. Öztop, A.Z. Şahin, An analysis of entropy generation through a circular duct with different shaped longitudinal fins for laminar flow, Int. J. Heat Mass Transfer 48 (2005) 171–181.
[7] A. Al-Sarkhi, E. Abu-Nada, Characteristics of forced convection heat transfer in vertical internally finned tube, Int. Comm. Heat Mass Transfer 32 (2005) 557–564.
[8] S.W. Chang, Heat transfer of orthogonal-mode reciprocating tube fitted with twisted-tape, Exp. Heat Transfer 13 (2000) 61–86.
[9] S.W. Chang, L.M. Su, Heat transfer of reciprocating helical tube fitted with full circumferential ribs, Int. J. Heat Mass Transfer 44 (2001) 3025–3042.
[10] T.H. Ko, Numerical investigation on laminar forced convection and entropy generation in a curved rectangular duct with longitudinal ribs mounted on heated wall, Int. J. Thermal Sci. 45 (2006) 390–404.
[11] S.W. Chang, T.-M. Liou, M.H. Lu, Heat transfer of rectangular narrow channel with two opposite scale-roughened walls, Int. J. Heat Mass Transfer 48 (2005) 3921–3931.
[12] Y. Mori, Y. Uchida, T. Ukon, Forced convective heat transfer in a curved channel with square cross section, Int. J. Heat Mass Transfer 14 (1971) 1787–1805.
[13] Y. Mori, W. Nakayama, Study on forced convective heat transfer in curved pipes (1st report, laminar region), Int. J. Heat Mass Transfer 8 (1965) 67–82.
[14] Y. Mori, W. Nakayama, Study on forced convective heat transfer in curved pipes (2nd report, turbulent region), Int. J. Heat Mass Transfer 10 (1967) 37–57.
[15] Y. Mori, W. Nakayama, Study on forced convective heat transfer in curved pipes (3rd report, theoretical analysis under the condition of uniform wall temperature and practical formulae), Int. J. Heat Mass Transfer 10 (1967) 681–695.
[16] S.V. Patankar, V.S. Pratap, D.B. Spalding, Prediction of laminar flow and heat transfer in helical coiled pipes, J. Fluid Mech. 62 (1974) 539–551.
[17] W.H. Lyne, Unsteady viscous flow in curved pipe, J. Fluid Mech. 45 (1971) 13–31.
[18] R. Zalosh, W.G. Nelson, Pulsating flow in a curved tube, J. Fluid Mech. 59 (1973) 693–705.
[19] H.A. Simon, M.H. Chang, J.C.F. Chow, Heat transfer in curved tubes with pulsatile fully developed laminar flow, ASME J. Heat Transfer 99 (1977) 590–595.
[20] N.J. Rabadi, J.C.F. Chow, H.A. Simon, Heat transfer in curved tubes with pulsating flow, Int. J. Heat Mass Transfer 25 (1982) 195–203.
[21] R. Akhavan, R.D. Kamm, A.H. Shapiro, An investigation of transition to turbulence in bounded oscillatory flows, part 1. Experiments, J. Fluid Mech. 225 (1991) 395–422.
[22] W.J. Jung, N. Mangiavacchi, R. Akhavan, Suppression of turbulence in wall-bounded flows by high frequency spanwise oscillations, Phys. Fluids A 4 (8) (1992) 1605–1607.
[23] A. Baron, M. Quadrio, Turbulent drag reduction by spanwise wall oscillations, Appl. Sci. Res. 55 (1996) 311–326.
[24] K.-S. Choi, B.R. Clayton, The mechanism of turbulent drag reduction with wall oscillation, Int. J. Heat Fluid Flow 22 (2001) 1–9.
[25] Editorial Board of ASME Journal of Heat Transfer, Journal of heat transfer policy on reporting uncertainties in experimental measurements and results, ASME J. Heat Transfer 115 (1993) 5–6.
[26] M.R.H. Nobari, K. Gharali, A numerical study of flow and heat transfer in internally finned rotating straight pipes and stationary curved pipes, Int. J. Heat Mass Transfer 49 (2006) 1185–1194.
[27] F.W. Dittus, L.M.K. Boelter, University of California, Berkeley, CA, Publ. Eng., vol. 2, 1930, p. 443.